Journal of MATERIALS RESEARCH

Article
DOI:10.1557/s43578-024-01350-4

Exploring the antimicrobial and anticancer activities of zinc doped nanohydroxyapatite prepared via ultrasonic-assisted method for bone tissue engineering

W. El Hotaby[1,a], A. M. Bakr[1], H. H. A. Sherif[1], Ahmed A. Soliman[2], Bahaa Hemdan[3]

[1] Spectroscopy Department, Physics Research Institute, National Research Centre, 33 El Bohouthst, Dokki, P.O. 12622, Giza, Egypt
[2] Pharmacognosy Department, Pharmaceutical and Drug Industries Research Institute, National Research Center, 33 El Bohouth St., Dokki, P.O. 12622, Giza, Egypt
[3] Water Pollution Research Department, Environmental and Climate Change Research Institute, National Research Centre, 33 El Bohouth St. Dokki, P.O. 12622, Giza, Egypt
[a] Address all correspondence to this author. e-mail: walid.mosad@gmail.com

Received: 30 November 2023; accepted: 22 April 2024; published online: 14 May 2024

The main purpose is to investigate the antimicrobial, biocompatibility properties, and anticancer activities of the nanohydroxyapatite (nHA) and Zn-doped nanohydroxyapatite prepared at different calcination temperatures. We utilized the wet precipitation method with the aid of ultrasonic waves. The impact of both the calcination temperature and Ca/Zn substitution assessed with spectroscopic techniques. The TEM images showed that nHA particles described by particles with a rod-like form transformed to a spherical shape with the Ca/Zn substitution. The antimicrobial features of the nHA samples suggested that higher concentrations of nHA exhibit stronger antimicrobial effects against the tested pathogens. Regarding in vitro cytotoxicity, assessments involving both human osteosarcoma (HOS) cells and human normal immortalized skin fibroblasts (BJ-1) cells indicate that the 20% Ca/Zn nHA sample exhibited the highest cell viability for BJ-1 cells, reaching 100%. Conversely, the nHA sample with a 10% Ca/Zn ratio induced the most pronounced cytotoxic effect in HOS cells.

Introduction

The deterioration of hard tissues resulting from accidents or diseases like malignant sarcoma tumors is a common health problem. In such cases, the damaged tissue, such as bone, needs to be replaced with a bone filler to provide an appropriate solution [1, 2]. The bone filler facilitates the rapid filling of the void and encourages the natural development of new hard tissues. Eventually, these fresh tissues become integrated into the skeletal system, which accelerates the healing process compared to situations where no bone filler is used [3–5].

Biomaterials are used to repair and reconstruct human bones and tissues that have been damaged by disease and can be bioactive, resorbable, or inert [6]. One remarkable substance that is particularly useful for replacing and reconstructing missing bone is hydroxyapatite (HA). With a Ca/P atomic ratio of 1.67, this calcium phosphate bioceramic has impressive biological characteristics. These include the following: maximum biodegradability, excellent biocompatibility, absence of immunological responses, absence of inflammatory response, and presence of osteoconductivity and osteoinductivity properties [7–9]. As a result, it has found extensive use in biomedical applications, including dental applications, and bone grafts in addition to drug delivery systems for controlled release [10, 11]. Additionally, HA exhibits excellent handling properties, such as easy synthesis, fabrication, and high stability [12].

Although hydroxyapatite (HA) only constitutes 70% of the usual natural bone components, the normal structure of human bone also comprises other substances, such as magnesium, sodium, carbonate, silicon, silver, and zinc [13, 14]. Zinc has received considerable attention for its capacity to improve cell viability, proliferation, and adhesion, as well as its antibacterial characteristics, which are advantageous in minimizing infections connected to implants [15]. A promising approach for

preventing bacterial infections is to develop implants or bone scaffolds using novel materials that possess both biocompatibility and antibacterial characteristics. Studies have presented that Zn exhibits higher antibacterial efficacy toward *Staphylococcus aureus* than *E. coli* [16], and Zn-doped Hap coatings are more efficient in combating *S. aureus* than *Bacillus cereus* [17–20]. In addition, zinc ions exert a significant influence on the proliferation of osteoblasts and the suppression of osteoclasts, making them very suitable for use in bone tissue engineering.

Scientists have been intrigued by the typical amount of zinc found in human tissues for a considerable time, and a report stated that it is approximately 5 mg per 100 g of liver and kidney tissue [21]. Due to its attributes as a divalent ion and a smaller ionic radius when compared to calcium (Ca^{2+}), this material has become increasingly prominent in various biomedical engineering applications. Its properties enable effortless substitution of Ca^{2+} ions, contributing to its preference in the field. Various forms of Zn^{2+}-doped HA can be utilized, such as coating materials, composite reinforcement agents, or components in tissue engineering scaffolds [22, 23].

Zinc ions are essential for cellular metabolism and development because they are present in so many cells as coenzyme factors. On the other hand, "Zn^{2+} interference" occurs when the intracellular Zn^{2+} level is too high and damages intracellular mitochondria, which in turn triggers an eruption of reactive oxygen species (ROS) and causes acute intracellular oxidative stress. "Zn^{2+} interference" has taken the lead in anticancer research as a result of its great safety profile and effective therapeutic effects [24]. Zn-based nanomaterial-promoted Zn^{2+} interference therapy has demonstrated distinct benefits and promising future uses in cancer treatment, despite the fact that it is still in its early stages [25]. The metabolic and nutritional benefits of Zn^{2+}, a biological metal ion, are vital for cell growth. Zinc ions, for instance, have the power to control gene expression, genomic stability, and energy consumption. A buildup of Zn^{2+} in an inappropriate way, however, will destroy cells permanently [26]. Research suggests that an excessive amount of Zn^{2+} can impede cellular glycolysis, resulting in the permanent obstruction of energy production. Additionally, it may act as an energy consumer in neurons [27]. Therefore, the presence of "Zn^{2+} interference" allows for the effective replacement of GOx-mediated tumor starvation therapy (ST) and overcomes GOx's limited efficacy caused by hypoxia in the tumor microenvironment (TME). Excessive levels of Zn^{2+} can cause a mitochondrial reactive oxygen species (ROS) burst by inhibiting the mitochondrial electron transfer chain (ETC). This, in turn, can elevate the oxidative stress levels in cancer cells. This increased stress can stimulate the activation of the proapoptotic Bax gene and facilitate the breakdown of mutant p53 protein in mutant p53 cancer cells [28]. As a result, nanoparticles derived from zinc can efficiently reduce tumor size, invasion, and metastasis, cause cancer cells to die off, and make tumors more responsive to chemotherapy [29]. Furthermore, an excess of Zn^{2+} has the potential to alter the process by which cancer cells die. Overexposure to zinc ions can trigger pyroptosis in cancer cells, which in turn causes them to enlarge, burst, and expel their contents (cytokines and proteins) [30].

There are numerous approaches have been progressed to synthesize nHA which have been conveyed in the literature such homogeneous precipitation, sol–gel, plasma spray, hydrothermal and ultrasonic spray freeze drying methods as well as [31] solid state and mechano-chemical methods. Between those methods, the wet chemical procedures are the most straightforward, simple, and cost-effective for creating HA, as they do not require expensive specialized equipment [32]. In a study conducted by Venkatasubbu and colleagues in 2011 [33], they prepared hydroxyapatite samples using the wet precipitation method. These samples included both pure HA and hydroxyapatite with varying concentrations of zinc, specifically 2%, 3%, 4%, and 5% by weight. In 2012, the group of scientists [34] synthesized HA at different calcination temperature (400, 500, 600, 700, and 800 °C) and hydroxyapatite with various zinc concentrations (2, 3, 4, 5 wt%) using the wet precipitation method.

Utilizing a chemical synthesis strategy that combines ultrasonic irradiation with a wet precipitation procedure, our study makes use of the ultrasonic-assisted wet precipitation method. This process is highly regarded because it produces nanoscale materials quickly and precisely with exact control over their characteristics. Materials or particles at the nanoscale are produced as a result of the procedure. Most importantly, it gives us precise control over critical reaction parameters like temperature and reaction time. The ability of the ultrasonic-assisted wet precipitation approach to shorten response times while improving our control over particle size and shape is one of its main advantages. In addition, it provides the ability for preparation of the materials at lower temperatures than traditional techniques, which makes it a useful approach for creating nanomaterials that may be used in a variety of applications.

As far as we know, there are no current publications discussing the impact of Ca/Zn substitution and calcination temperature on nanohydroxyapatite (nHA) synthesized through ultrasound-assisted wet precipitation. This study encompasses several significant stages. It offers insights into how varying calcination temperatures and calcium/zinc (Ca/Zn) substitution affect the crystallinity, morphology, and other properties of nHA, including its antibacterial and cytotoxic characteristics. First, we address the simple and affordable synthesis of nHA by wet precipitation with ultrasound assistance. We then examine the effects of calcination temperature and Ca/Zn substitution on the nHA. The third stage involves a thorough examination of the produced samples' morphology and structure. Finally, in order to meet the clinical necessities for use in bone tissue

creation and replacement, we investigate the nHA's antibacterial and cytotoxic qualities.

Results and discussions

FTIR spectroscopy

Figure 1(a, b, c, and d) displays the FTIR spectra of nHA powders synthesized at different temperatures (100 °C, 200 °C, 300 °C, and 400 °C). The FTIR spectra of nHA have a broad peak at 3436 cm^{-1}, indicating the stretching vibrations of the hydroxyl (OH) group [35]. The peaks observed at 1097 cm^{-1}, 1055 cm^{-1}, and 960 cm^{-1} are associated with the stretching modes of the phosphate group $(PO4)^{-3}$ in hydroxyapatite. The peaks at 1055 cm^{-1} and 960 cm^{-1} correspond to the asymmetric (v1) stretching vibration of the PO group in hydroxyapatite [36–38]. On the other hand, the peak at 1097 cm^{-1} is related with both symmetric and asymmetric stretching vibration modes of the $(PO4)^{-3}$ group [39, 40]. Distinct absorption peaks at 869 cm^{-1} and 634 cm^{-1} were found, corresponding to the vibrations of CO_3^{-2} and OH, respectively [41]. The bands observed at 603 cm^{-1}, 565 cm^{-1}, and 468 cm^{-1} correspond to the bending modes of the PO (v4) in the $(PO4)^{-3}$ group [42]. The findings indicated that there was no significant disparity in the nHA samples generated at varying temperatures. The results are consistent with the findings of Sibte et al. 2014 [43] and Mahmutoglu et al. 2023 [44], which demonstrate that there were no noticeable changes in the FTIR spectra of nHA samples prepared at different calcination temperatures within the same range.

As reported in the literature, the peaks at 1097 cm^{-1}, 1055 cm^{-1}, and 960 cm^{-1} (which represent stretching vibration of PO_4 group) are affected by the Zn substitution. These peaks are supposed to be broader and diminish as the concentration of Zn ions increases. However, in our experiment, the amount of Zn ion substitution is not sufficient to cause these changes in the FTIR spectra. Therefore, the spectra of the samples with Zn substitution show no significant spectral changes." In addition, the influence of Ca/Zn substitution on the nHA samples was found to be insignificant upon careful examination.

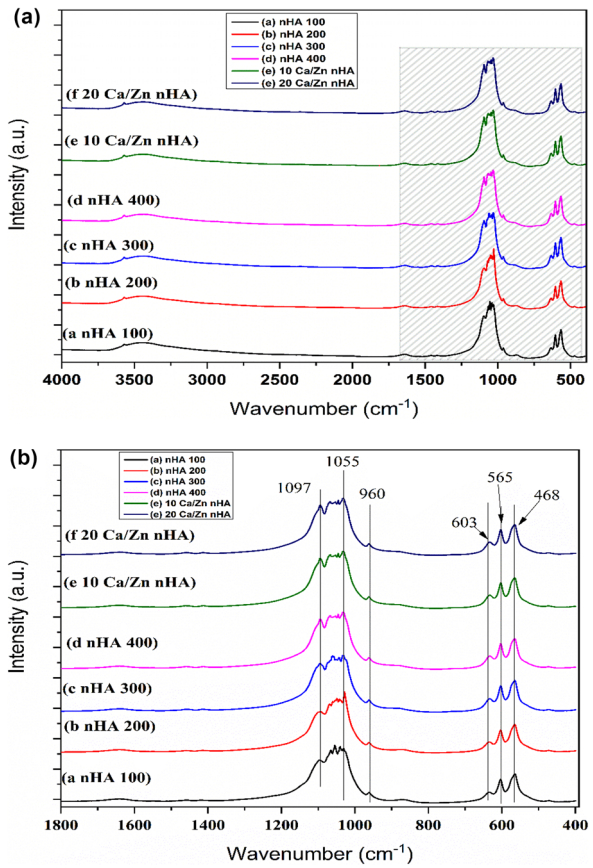

Figure 1: (a) FTIR spectrum of (a–d) nHA powder prepared under different temperature 100 °C, 200 °C, 300 °C, and 400 °C, respectively. (e, f) FTIR spectrum of nHA with prepared by substituting Ca with Zn with different percentages, i.e., 10% and 20%, respectively. (b) magnified FTIR spectrum of (a–d) nHA powder prepared under different temperature 100 °C, 200 °C, 300 °C and 400 °C, respectively. (e, f) FTIR spectrum of nHA with prepared by substituting Ca with Zn with different percentage, i.e., 10% and 20%, respectively.

X- ray diffraction

The XRD patterns nHA synthesized at different temperatures (100 °C, 200 °C, 300 °C, and 400 °C), and (b) the nHA synthesized at 400 °C is present in Fig. 2(a) while XRD patterns of 10 Ca/Zn nHA and Ca/Zn 20% substitution of nHA are demonstrated in Fig. 2(b). The XRD diffraction patterns of nHA were extremely similar to that of the stoichiometric reference for hexagonal $Ca_{10}(PO_4)_6(OH)_{26}$ (JCPDS No. 96-101-1243). In all the samples examined, the (021), (211), (041), and (230) crystallographic planes displayed higher peak intensities compared to other planes. Obviously, there was no significant change in the lattice structure of nHA arising from different calcination temperatures [Fig. 2(a)].

In the case of different Ca/Zn substitutions of nHA [Fig. 2(b)], with the increase of Zn concentration, the crystallinity decreased and broader XRD peaks were obtained. This observation is consistent with the results presented by Uysal et al. in 2021 [22], where they attributed the decrease in crystallinity following Zn/Ca substitution to the variance in ionic diameters between Zn and Ca. Specifically, since the ionic diameters of Zn^{2+} ion and Ca^{2+} ion are 0.074 nm and 0.099 nm, respectively; therefore, the crystal size decreases as a result of the replacement.

In order to knowing more facts around the crystal size of the prepared materials, Scherrer equation is used as follows:

$$D = \frac{\kappa\lambda}{\beta\cos\theta} \quad (1)$$

In the Scherrer equation, which is used to calculate the average crystal size (D), λ represents the X-ray wavelength, β is the width of the diffraction peak)FWHM(in radians, θ is the Bragg

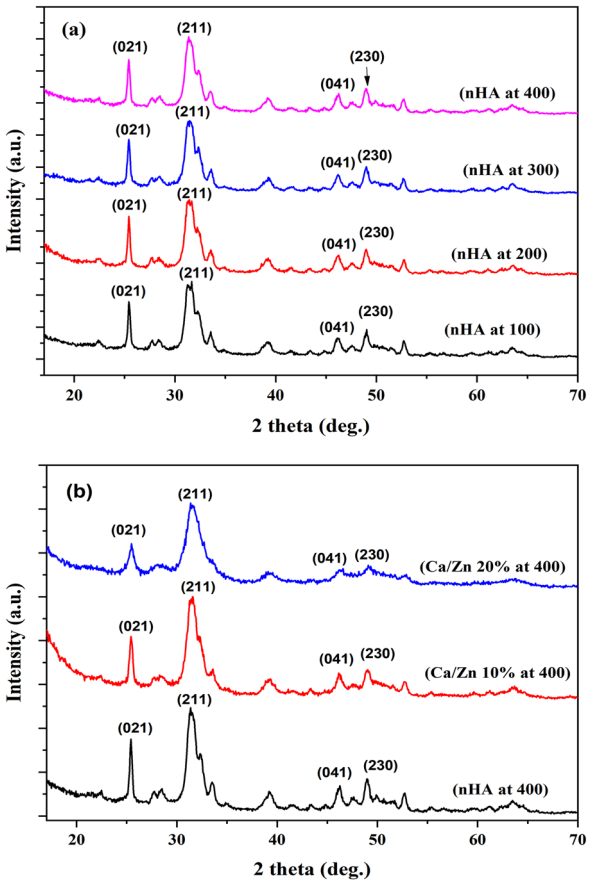

Figure 2: The XRD patterns of (a) the nHA synthesized at different temperatures (100 °C, 200 °C, 300 °C and 400 °C), and (b) the nHA synthesized at 400 °C, Ca/Zn 10% substitution of nHA and Ca/Zn 20% substitution of nHA.

TABLE 1: The crystal size of the prepared samples using Scherrer equation.

Sample	Average crystal size (nm)
100 °C	15 ± 0.70
200 °C	14 ± 0.65
300 °C	13 ± 0.83
400 °C	12 ± 0.4
10% Zn	10 ± 0.56
20% Zn	5 ± 1.12

angle, and κ is the Scherrer constant, which depends on the crystalline morphology.

As shown in Table 1 which described the results of crystal size of the all samples using Scherrer equation. It's clear to seen that there are slight changes that could be detected in the crystal size due to the increasing in calcination temperature, while the addition of zinc ions in the crystal structure causing a significant decreasing in crystal size especially for 20% Zn-loaded samples, those decreasing in the crystal size could be resulted from the smaller size of Zn ions compared to Ca ions. This conduct could be owing to the elevation the number of nucleation sites caused by the presence of Zn2 + ions Zn^{2+} ions which repressed the crystallites' growth and subsequently reduced the crystallinity of the nHA. These results are harmonious with the results previously reported by Cleibson et al. 2021 [45].

Scanning electron microscopy

SEM was used to investigate the effect of temperature and ca/Zn substitution on nanoparticle particle size and morphology. Figures 3(a) and 4(b) illustrate that the powder samples synthesized at 400 °C temperatures and 20% Ca/Zn substitution, respectively, are spherical in shape. Both powder samples exhibit particle sizes within the range of 40–60 nm. Close examination of the Figure also reveals that Ca/Zn substitution seems to have discernible impact on the particle morphology of nHA.

The nHA samples were analyzed using EDAX to evaluate their fundamental structure. The chemical constituents and uniformity of a substance greatly influence its ability to interact with living organisms and its effectiveness in killing microorganisms. Figure 3(c, d) exhibits the EDAX spectra of nHA 400 and 20 Ca/Zn nHA samples. The EDAX analysis primarily indicates the presence of calcium (Ca), phosphorous (P), and zinc (Zn) in the produced samples. The EDAX analysis yielded Ca/P and (Ca + Zn)/P ratios of 1.64 and 1.88 for the nHA 400 and 20 Ca/Zn nHA samples, respectively. These readings closely approximate the stoichiometric assessment of 1.67, which represents the theoretical value. The observed correlation of the Ca/P ratio not only verifies the successful formation of nanohydroxyapatite (nHA), but also suggests the generation of high-quality nHA powders.

Transmission electron microscope

The nanoparticle size of the produced particles can be observed through transmission electron microscopy (TEM). Figure 4(a, b) shows the TEM micrograph of nHA synthesized at 400 °C and 20% Ca/Zn substitution, respectively. The TEM images showed that the nHA particles described by a rod-like form (typically 12 nm in diameter and 70 nm in length) transformed to a spherical shape of about 10 nm with the Ca/Zn substitution. Some of the particles appear to accumulate as a result of crystal fusion during the sintering process. The diffraction patterns serve as clear proof of the underlying crystal structure.

Zeta potential

The examination of zeta potential is expected to provide insights into the impact of temperature and Ca/Zn substitution on the surface charge of nHA when it is dispersed in

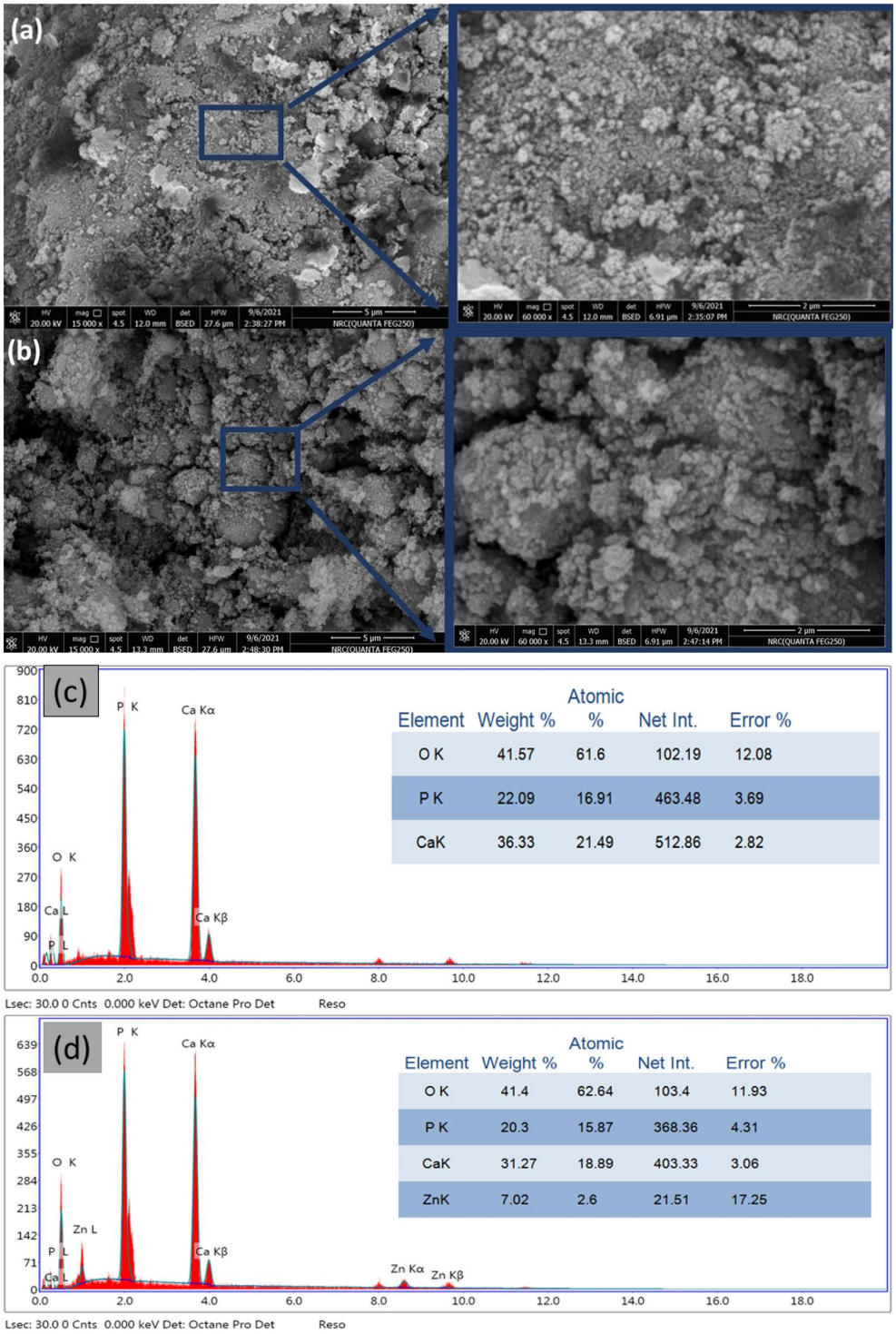

Figure 3: (a–d) SEM images of nHA 400, and 20 Ca/Zn nHA (scale bar = 2 µm) and EDAX results, respectively.

distilled water. It is important to mention that the surfaces of all nHA samples exhibit a negative charge, as illustrated in Table S1. This negatively charged surface of nHA could have potential applications after implantation in bone, as suggested [46]. As the preparation temperature increases, there is a noticeable decline in the zeta potential value of nHA. Specifically, the zeta potentials for nHA synthesis at 100 °C, 200 °C, 300 °C, and 400 °C are recorded as – 20.18 mV, -26.05 mV, – 41.77 mV, and – 44.33 mV, respectively. Notably, the zeta potential of the 10% Ca/Zn nHA exhibits a shift from – 44.33

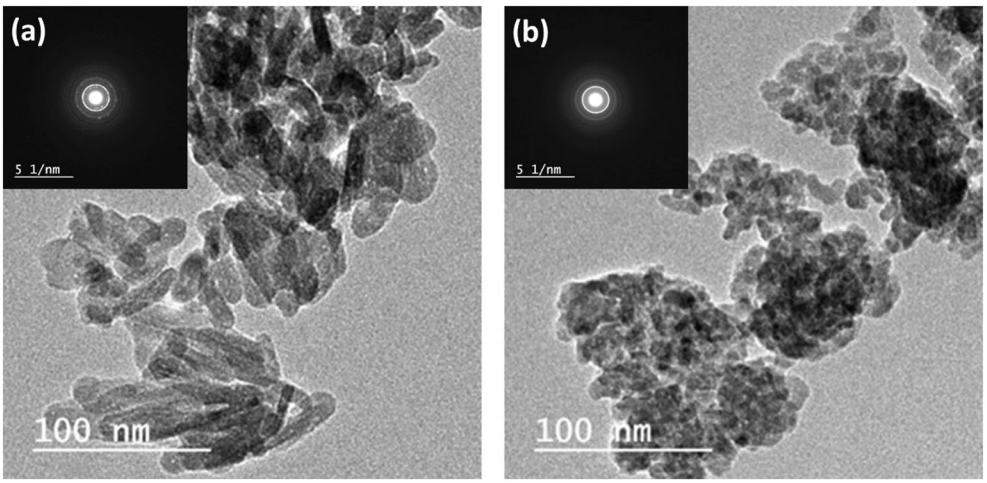

Figure 4: Transmission electron microscopy of (a) nHA 400°C and (b) 20 Ca/Zn nHA (scale bar = 100 nm).

to − 25.20 mV before returning to its original value at a 20% substitution percentage.

Antimicrobial assays of tested nanostructured materials

Figure S1 provides the estimated width of ZOI values obtained through the disk diffusion assay for various nanostructured materials tested against specific pathogenic microbes. For the pathogenic microbe *P. aeruginosa*, the ZOI values are as follows: nHA 100 (0), nHA 200 (0 mm), nHA 300 (10 mm), nHA 400 (18 mm), 10 Ca/Zn nHA (24 mm), and 20 Ca/Zn nHA (21 mm). These values indicate the diameter of the inhibition zone observed around the disk containing the respective nanostructured material. A larger ZOI value signifies a stronger inhibitory effect against the growth of *P. aeruginosa*. For the pathogenic microbe *S. Aureus*, the ZOI values are as follows: nHA 100 (0 mm), nHA 200 (0 mm), nHA 300 (8 mm), nHA 400 (15 mm), 10 Ca/Zn nHA (22 mm), and 20 Ca/Zn nHA (17 mm). Similarly, increasing values indicate an increased inhibitory effect against *S. aureus*. The ZOI values for *C. albicans*, a pathogenic fungus, are as follows: nHA 100 (0 mm), nHA 200 (0 mm), nHA 300 (7 mm), nHA 400 (13 mm), 10 Ca/Zn nHA (19 mm), and 20 Ca/Zn nHA (15 mm). As the ZOI values increase, it indicates a stronger inhibitory effect on the growth of *C. albicans*. Lastly, for *A. niger*, the ZOI values are as follows: nHA 100 (0 mm), nHA 200 (0 mm), nHA 300 (6 mm), nHA 400 (11 mm), 10 Ca/Zn nHA (17 mm), and 20 Ca/Zn nHA (14 mm). Increasing ZOI values indicate a greater inhibitory effect against *A. niger*. Overall, the results suggest that higher concentrations of nanostructured materials, such as nHA and Ca/Zn nHA, generally lead to larger inhibition zones, indicating increased antimicrobial activity against the tested pathogenic microbes.

Comparing the results within the table, it can be observed that as the concentration of nHA (nanohydroxyapatite) increases from 100 to 400, the width of the inhibition zone generally increases for all tested microbes. This suggests that higher concentrations of nHA exhibit stronger antimicrobial effects against the tested pathogens. Furthermore, comparing the effects of nHA with the effects of Ca/Zn (calcium/zinc) nanomaterials, it is evident that the Ca/Zn nanocomposites generally have wider inhibition zones compared to nHA for all tested microbes. This indicates that the Ca/Zn nanomaterial possesses enhanced antimicrobial properties compared to nHA. To compare these results with previous findings, it would be necessary to refer to previous studies or experiments that have evaluated the same or similar nanostructured materials against the same pathogens using the disk diffusion assay. By comparing the ZOI values obtained in this study with the previous results, it would be possible to determine if there are any significant differences or similarities in the antimicrobial activity of the tested materials.

Dosages and time inhibitory effect

From the results of zone of inhibition assay could be indicated that no potential ZOI was detected for nHA 100 and nHA 200 nanomaterials, while other nanomaterials including nHA 300, nHA 400, 10 Ca/Zn nHA, and 20 Ca/Zn nHA were selected for further antimicrobial studies since they have a strong antimicrobial effect against targeted microbes. The time- and dose-kill kinetics assay was also conducted to assess the antimicrobial activity of these compounds against different bacterial and fungal strains. This assay allows for the determination of the time and concentration required to achieve antimicrobial activity. The inhibitory effect of four various dosages of each selected nanomaterials within exposure time was subjected to inactivate the 6-log cell counts of each tested species (Figs. 5, 6, 7, 8).

The findings depicted in Fig. 5 reveal that the nHA 300 nanomaterial exhibited effectiveness primarily against *P. aeruginosa* and *S. aureus*. However, it demonstrated limited efficacy against the tested fungal species, which appeared to be more resistant to its antimicrobial effects. The study demonstrates that the effective dosage of nHA 300 nanomaterial for eliminating *P. aeruginosa* and *S. aureus* mutans was found to be 90 µg/mL, and this dosage achieved a significant reduction in microbial viability within 10 to 15 min (as depicted in Figure S2). However, it's important to note that this same dosage of 90 µg/mL was found

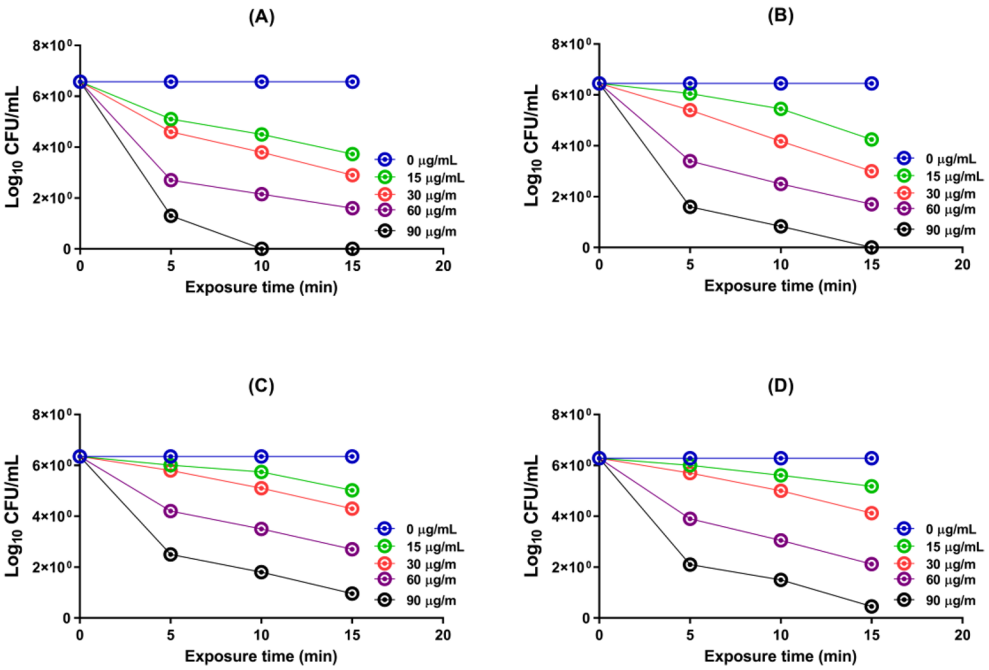

Figure 5: The (MIC) values of the nHA 300 nanomaterial were determined for four investigated microbiological species: (A) *P. aeruginosa*, (B) *S. aureus*, (C) *C. albicans*, and (D) *A. niger*.

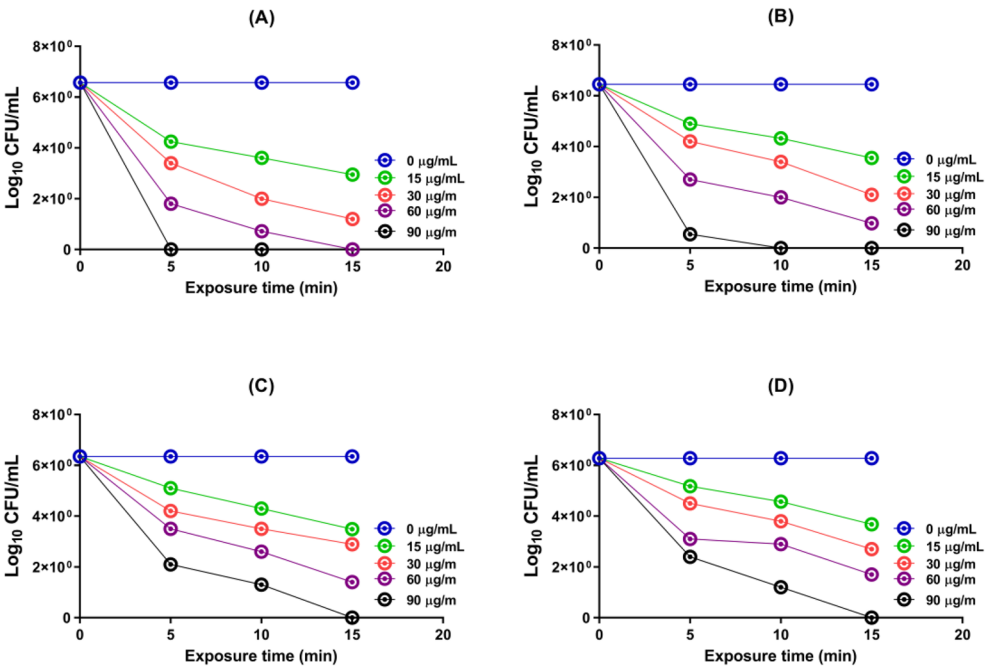

Figure 6: The (MIC) values of the nHA 400 nanomaterial were determined for four investigated microbiological species: (A) *P. aeruginosa*, (B) *S. aureus*, (C) *C. albicans*, and (D) *A. niger*.

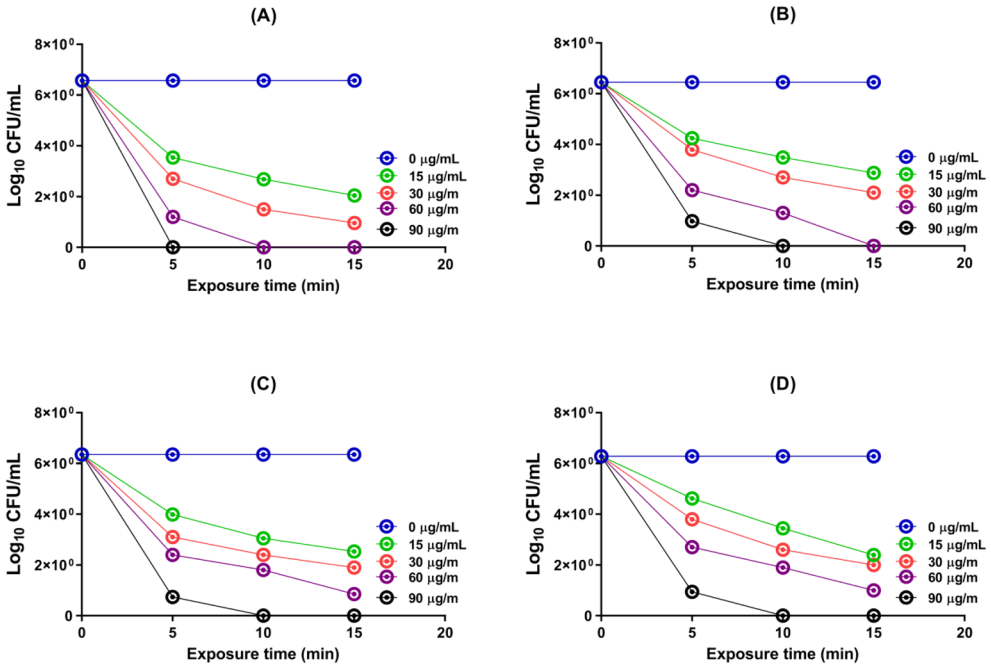

Figure 7: The (MIC) values of the 10 Ca/Zn nHA nanomaterial were determined for four investigated microbiological species: (A) *P. aeruginosa*, (B) *S. aureus*, (C) *C. albicans*, and (D) *A. niger*.

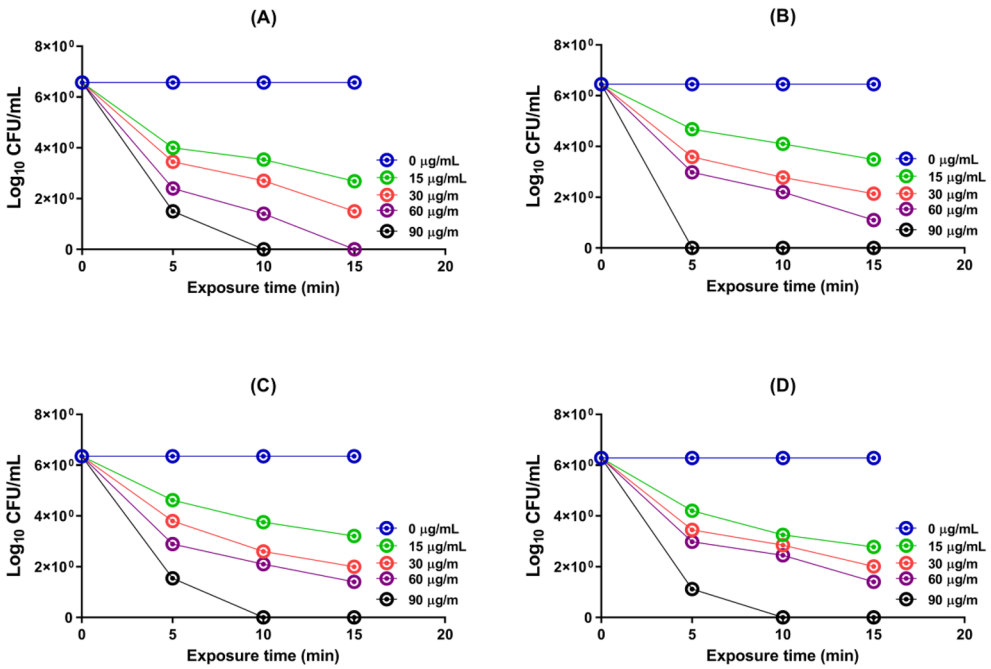

Figure 8: The (MIC) values of the 20 Ca/Zn nHA nanomaterial were determined for four investigated microbiological species: (A) *P. aeruginosa*, (B) *S. aureus*, (C) *C. albicans*, and (D) *A. niger*.

to be ineffective against the tested fungal species, suggesting that these fungal strains are more resilient to the antimicrobial properties of the nanomaterial.

The MIC dosage values of nHA 400 nanomaterial were found for four different microbial strains, as shown in Fig. 8. The results showed that when the nanomaterial was present at a concentration of 90 µg/mL, it completely prevented the growth of P. aeruginosa, S. mutans, C. albicans, and A. niger. This suppression occurred at several time intervals, specifically after 5, 10, and 15 min of exposure.

Figure 9 provides a clear explanation of the minimum inhibitory concentration (MIC) values of 10 calcium/zinc nanohydroxyapatite (Ca/Zn nHA) materials for the four microbial strains that were investigated. The experiment found that a concentration of 60 µg/mL of 10 Ca/Zn nHA was required to totally eliminate P. aeruginosa within a 10-min period. Similarly, the proliferation of S. aureus was suppressed following a 15-min exposure to 60 µg/mL of 10 Ca/Zn nHA. In addition, the proliferation of C. albicans and A. niger was entirely suppressed when exposed to a concentration of 90 µg/mL of 10 Ca/Zn nHA, which was accomplished in a span of 10 min.

The results presented in Fig. 8 provide information about the MIC values of 20 Ca/Zn nHA for four tested microbial strains. The MIC values indicate the lowest concentration of 20 Ca/Zn nHA required to completely eradicate or inhibit the growth of the respective microbial strains. According to the investigation, a concentration of 60 µg/mL of 20 Ca/Zn nHA was found to be necessary for the complete eradication of *P. aeruginosa* within a 15-min exposure period. For *S. aureus*, a 5-min exposure to a concentration of 60 µg/mL of 20 Ca/Zn nHA was required for complete eradication. In the case of *C. albicans* and *A. niger*, a concentration of 60 µg/mL of 20 Ca/Zn nHA was sufficient to inactivate their growth within a 15-min exposure period. These results indicate the antimicrobial efficacy of 20 Ca/Zn nHA against the tested microbial strains, with specific dosage and exposure time requirements for complete eradication or growth inactivation.

Antimicrobial mechanism

The zinc-dotted nanohydroxyapatite (nHA) integrates substantial processes in antibacterial movements. The zinc ions (Zn^{2+}) are then lost from the nanoscale hydroxyapatite network because of the dissolution or degradation of the network. Zinc ions play a critical function in the antimicrobial impact of such promising antimicrobial materials. Zinc ions can antagonize bacterial cellular energy production, producing free radicals, such as superoxide radicals (O_2^-) and hydroxyl radicals ($OH\cdot$), which may induce oxidative damage to biological molecules in bacterial cells (as shown in Fig. 9). Zinc ions engage with the cell membrane of bacteria and make complexes with membrane proteins, which increase the membrane permeability and cause an untimely release of intracellular contents and interference with the cell structures and inviolability of the bacterial cells in free process. Further, zinc ions interfere with the structure and functions of bacterial enzymes and can thus damage several vital intracellular functions of the microorganism. Zinc ions bind to the redox sites of one of the main elements bacteria require for biological functioning, such as iron (Fe^{2+}) and manganese (Mn^{2+}), interfering with the process. Zinc ions have immunomodulation features suitable for modifying the immune response and the instances of bacterial infections. The concentration, the dimension of particles, the surface quality, and bacterial species control Zn-NP nanohydroxyapatite's antimicrobial mechanism [47, 48].

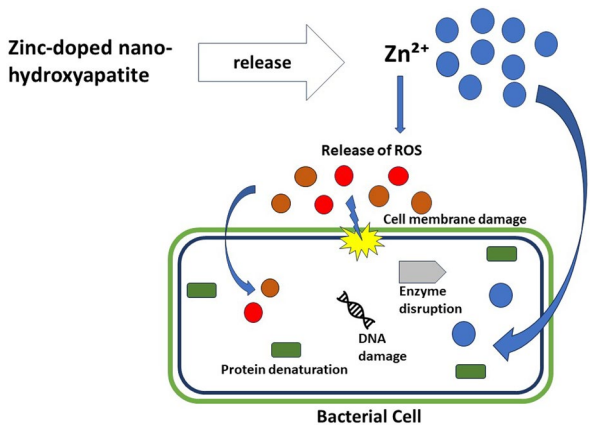

Figure 9: Schematic diagram shows the antimicrobial mechanism of zinc-doped nanohydroxyapatite.

In vitro cytotoxicity

To assess the biocompatibility of the prepared nHA on normal cells, we conducted the cytotoxicity tests on human normal immortalized skin fibroblasts (BJ-1) cells as depicted in Fig. 10a. The samples include nHA prepared with different calcination temperatures and with various Ca/Zn substitutions. Among these samples, the 20% Ca/Zn nHA exhibited the highest cell viability (100%) when tested against BJ-1 cells. When examining nHA prepared at different calcination temperatures, the cell viability for BJ-1 followed a distinct trend, decreasing as the temperature rose, but with a sudden increase at the highest temperature tested, 400 °C. Specifically, viability dropped from 98.7% to 90.8% at nHA 300 °C but then rebounded to 93.7% at nHA 400 °C. When evaluating various Ca/Zn substitution ratios, it was evident that the 20% Ca/Zn nHA demonstrated higher cell viability for BJ-1 in comparison with the 10% Ca/Zn nHA, resulting in complete survival of BJ-1 cells. It can be concluded from those results that all the prepared samples are biologically safe materials and could be used in contact with healthy human cells without any measurable side effects.

On the other hand, to investigate of the anticancer effect of prepared nHA samples, the cytotoxicity tests were performed on the bone cancer cells (HOS), as shown in Fig. 10(a). Subsequently, IC50 values were determined and presented in Fig. 10(b). The most substantial cytotoxic effect was observed in HOS cells when exposed to the nHA sample with a 10% Ca/Zn nHA ratio, which killed about 63.6% of the cancer cells. Regarding different calcination temperatures of nHA samples, HOS cell cytotoxicity increased from 38.3% to 59% at nHA 300 °C but

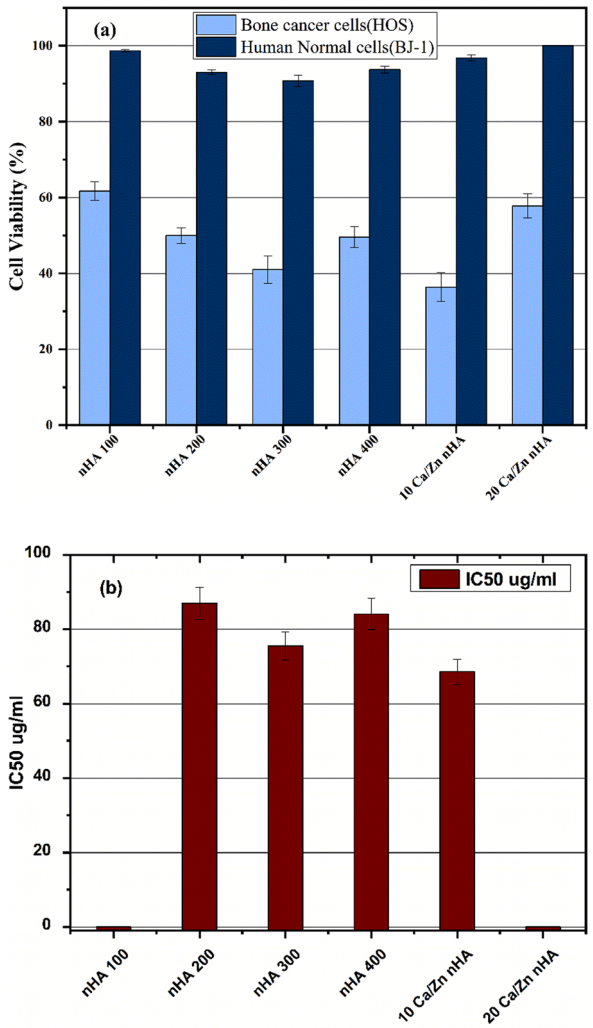

Figure 10: Cell viability test against human normal cells (BJ-1) and Bone cancer cells (HOS).

subsequently decreases to 50.4% at nHA 400 °C. When evaluating various Ca/Zn substitution ratios, the 10% and 20% Ca/Zn nHA sample resulted in the killing 63.6% and 42.2% of the cancer cells (HOS), respectively.

IC50 values, denoted in μg/mL, were calculated to signify the concentration of the prepared nHA necessary for a 50% reduction in cell viability. The findings demonstrate that the lowest IC50 values were associated with the nHA 100 and 10% Ca/Zn nHA samples. In contrast, both the nHA 200 and nHA 400 samples displayed the highest IC50 values, measured at 87.0 μg/mL and 84.1 μg/mL, respectively.

In conclusion, the biocompatibility of nanohydroxyapatite (nHA) preparations on normal cells, represented by BJ-1 cells, showed promising results, with the 20% Ca/Zn nHA demonstrating the highest cell viability. Conversely, the anticancer effect of nHA on bone cancer cells (HOS) indicated significant cytotoxicity, particularly with the 10% Ca/Zn nHA sample. The findings regarding the biocompatibility and cytotoxicity of nanohydroxyapatite (nHA) preparations have significant implications for bone tissue engineering applications. The high cell viability observed in normal cells (BJ-1) when exposed to nHA suggests that it is biocompatible and suitable for use in scaffolds or coatings for bone implants. The ability of nHA to promote cell survival and potentially enhance bone regeneration is promising. Additionally, the cytotoxic effects observed on cancer cells (HOS) indicate that nHA may have potential applications in targeted cancer therapies for bone cancers. By selectively targeting cancer cells while sparing healthy bone cells, nHA could help in developing more effective and less harmful treatments for these types of cancer.

Furthermore, the remarkable antimicrobial properties demonstrated by the 10% Ca/Zn nHA nanomaterial against a range of bacterial species (both Gram-positive and Gram-negative) as well as fungal strains further enhance its potential applications. This antimicrobial activity could be leveraged in various medical devices and implants to prevent infections, which are a common complication in orthopedic surgeries and other medical procedures. Overall, the comprehensive findings on nHA's biocompatibility, cytotoxicity, and antimicrobial properties suggest a wide range of potential biomedical applications. Additional research is necessary to fully comprehend the mechanisms that underlie these effects and to improve the utilization of nanohydroxyapatite (nHA) in bone tissue engineering, cancer therapy, and antimicrobial applications.

Conclusion

In this current investigation, we synthesized nHA and Ca/Zn nHA by applying the ultrasound-assisted wet precipitation method and then confirmed their formation through various analytical techniques. The analysis by FTIR and XRD revealed that there were no significant alterations in the lattice structure of nHA due to variations in calcination temperature. However, when we examined different Ca/Zn substitutions in nHA, we observed a decrease in crystallinity and broader XRD peaks as the Zn concentration increased. Additionally, a remarkable decreasing in crystal size with Zn ions substitution. Interestingly, Ca/Zn substitution appeared to influence the particle morphology of nHA.

The antimicrobial activity results have shown that the 10% Ca/Zn nHA nanomaterial possesses remarkable antimicrobial properties, especially when tested against both Gram-positive and Gram-negative bacterial species, as well as fungal strains. Consequently, the 10% Ca/Zn nHA nanomaterial demonstrates exceptional inhibitory capabilities. Furthermore, it is important to mention that the nHA sample containing a 10% Ca/Zn ratio caused the most notable cytotoxic impact on HOS

cells. These results are promising for future use in the field of bone replacement and tissue engineering.

Materials and methods

Materials

$CaCl_2$, Na_2HPO_4, and Na-OH, which served as sources of Ca^{2+}, PO_4^{3-}, and OH–, respectively. Zinc acetate dihydrate $Zn(CH_3CO_2)_2.2H_2O$ was used as Zn^{2+} source. Utilizing Hielscher ultrasound technology, we used a UP50H ultrasonic processor (50 W, 30 kHz). We employed our reagents without further purification, regardless of whether they were analytical grade or the purest available. We dissolved the compounds in Millipore deionized water to create aqueous solutions.

Synthesis of zinc-nanohydroxyapatite

With the use of a wet precipitation technique in conjunction with ultrasonic irradiation [49], this work sought to create zinc-substituted nanohydroxyapatite (Zn-HA) with varied Zn concentrations ($x = 0$, 1, and 2 mol%). There were several crucial phases in the synthesizing process. First, 400 ml of a 0.2 M $CaCl_2$ solution underwent an hour-long ultrasonography treatment. A milky suspension formed as a consequence of adding a 0.12 M solution of Na_2HPO_4 (400 ml) dropwise at a rate of 200 ml/h using a syringe pump, stirring, and continuous ultrasonic irradiation using ultrasonic prop (50 kW) while maintaining ultrasonication. Throughout the procedure, the pH of the suspension was continuously checked and modified to stay between 9.5 and 10.5. After that, a white precipitate developed, and a further hour of ultrasonic irradiation was administered. In order to add zinc substitution, the $CaCl_2$ solution was mixed with precisely the right quantity of dissolved zinc acetate in deionized water, following the chemical formula. Centrifugal filtering was used to create a homogenous solution, which was then rinsed with deionized water twice, washed with ethanol once, and washed again with deionized water. The white precipitates were then allowed to dry at 100 °C for the whole night. The samples were dried, then finely powdered before being placed into ceramic boats. These materials were thermally treated for 4 hours at a rate of 10 °C/10 min in an oven with temperatures ranging from 100 to 400 °C. The resulting powders were calcined and then crushed into very small particles so they could be used for further analysis and applications. Figure 11 provides an overview of this process visually.

The constituents, temperature of preparation, and symbolization of prepared samples are shown in Table 2.

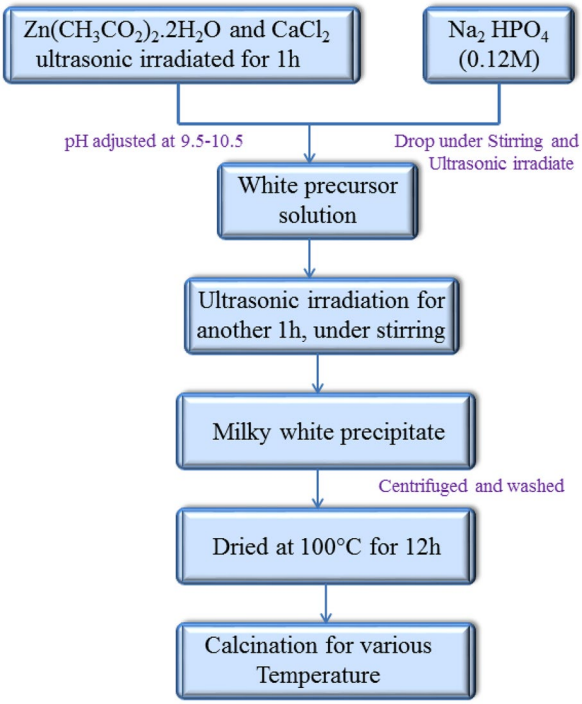

Figure 11: Flow chart of the preparation procedure.

TABLE 2: Constituents, temperature of preparation, and symbolization of prepared samples.

Sample symbol	Compositions and constituents Zn content (%)	Temperature (°C)
nHA 100	–	100
nHA 200	–	200
nHA 300	–	300
nHA 400	–	400
10 Ca/Zn nHA	10	400
20 Ca/Zn nHA	20	400

Characterization

FTIR analysis was conducted using an FTIR spectrometer (type A FT/IR Vertex 8000 Bruker Optiks) with a spectral resolution of 4 cm^{-1} in the vibrational wavenumber range of (400–4000 cm^{-1}), using ATR unit with diamond crystal.

The generated samples were subjected to a thorough investigation employing sophisticated analytical methods, including their structure, crystallinity, surface morphology, and particle properties. Cu-Kα radiation with a wavelength of 0.15418 nm was used in an Empyrean diffractometer system Broker D8 Advance, Germany, to conduct X-ray diffraction (XRD) investigation, with a 2θ range that covered 10° to 70° the XRD instrument ran at 40 kV and 40 mA. After obtaining the diffraction

peaks, the materials' crystalline patterns were determined by comparing them with the ICDD (JCPDS) standards.

Using high-resolution scanning electron microscopy (FE-SEM), the surface morphology and particle size were examined in detail. A Holland-made FEI Quanta FEG 250 system running at a 20 kV applied voltage was used for this investigation. A thin coating of gold was applied to the samples before SEM imaging in order to make it easier to see the borders and morphology of the grains. Moreover, SEM imaging was used to analyze the particle size.

The characteristics and crystallinity of the nanoparticles were further examined using high-resolution transmission electron microscopy (HR-TEM) with a Joel model JEM-2100 operating at 200 kV. The particles were dispersed in water and applied onto TEM grid. The dispersion was let to dry naturally at room temperature before being examined.

A particle size analyzer (Nano-ZS, Malvern Instruments Ltd., UK) was also used to measure the particles' zeta potential, average diameter, and size distribution. In order to guarantee precise measurements of the zeta potential and particle size distribution, the samples were subjected to sonication for at least 15 to 30 min before evaluation. All of these investigations together provide a thorough knowledge of the morphological and structural properties of the materials that were synthesized.

Antimicrobial assay

Microorganisms used

The antimicrobial performance of six nanostructured materials (nHA 100, nHA 200, nHA 300, 10 Ca/Zn nHA, and 20 Ca/Zn nHA) was assessed against four different types of microorganisms including *Pseudomonas aeruginosa, Staphylococcus*, *Candida albicans*, and *Aspergillus niger*. The bacterial strains were cultivated on a nutrient-rich medium until they reached the log phase stage of development to ensure optimum proliferation. Each strain's inoculum was made by acquiring, cleaning, and re-suspending the bacteria in sterile saline. On the other hand, fungi strains were grown on a liquid medium or on suitable agar plates. Mycelial pieces were collected, cleaned, and re-suspended to generate the fungal inoculum. To create the bacterial inoculum, all microbial strains were then grown in Trypicase Soya broth (TSB) and kept in an incubator for 24 h at 37 °C. Sabaroud dextrose agar (SDA) media were applied for cultivating yeast and mold species. This methodical approach was implemented to ensure homogeneity throughout various duplications and examinations. Optical density data were used to calculate the ultimate cell density needed for the experiment. The standardized inoculum was then modified to fit the 0.5 McFarland standards. A pair of standard drugs, 100 µg each of ciprofloxacin and nystatin, was administered as positive controls [50].

Examination of inhibition zone

In the present study, four microbial species (*P. aeruginosa, S. aureus, C. albicans*, and *A. niger*) and agar diffusion experiments (both disk and well techniques) were performed to investigate the antimicrobial activity of the tested nanostructured materials. While SDA medium was used for the fungal species, Muller Hinton agar (MHA) media were created and positioned onto Petri plates with a thick layer for the bacterial species. Aseptically, 100 µL of newly produced cultures of every microbial species was distributed throughout the agar layer. In the disk diffusion experiment, 100 µL of the tested extract was poured onto 6 mm diameter disks, which were then put on the surface of agar plates infected with the desired microorganisms. Subsequently, the plates were incubated at the ideal temperature for bacterial species (37 °C for 24 h) and fungal species (28 °C for 48–72 h) [51]. The zones of inhibition (ZOI) that formed on the medium after the incubation time were measured using a Vernier caliper and reported as diameters in millimeters (mm).

Cell viability inactivation assays

The inactivation kinetics of the materials under investigation was assessed using a macro-dilution test, which considered both the variables of dosage and time. The study employed a standard stock solution for the experimental procedure. The optimal dosage was determined by evaluating the effectiveness of the antimicrobial agent against the specific pathogens being studied. For each test, a sterile test tube containing 10 mL of sterile MHB and SDB media was prepared. A volume of 0.5 mL of a recently prepared culture of the target bacterium was introduced into the tube. While the remaining tubes were contaminated with different concentrations (15, 30, 60, and 90 µg/mL) of the tested materials, a single tube was designated as the control and remained free from contamination. The tubes were subsequently subjected to incubation for different durations, ranging from 5, 10, and 15 min. After each exposure period, a volume of one mL was taken from each tube and subjected to serial dilution following treatment with the tested ingredients. This was done to determine the number of viable microbial cells remaining. The plate-count method was employed to ascertain the CFU/mL by quantifying the population of viable microorganisms [52].

Cytotoxicity test

Cell culture

The HOS (human osteosarcoma) cells and BJ-1 (human normal immortalized skin fibroblasts) were cultured in DMEM F12 medium supplemented with 10% fetal bovine serum. The cells were incubated at 37 °C in an atmosphere of 5% CO_2 and 95% humidity. The cells were grown in subculture using a 0.15% trypsin–versine solution. The cell lines were acquired from the

Karolinskacenter, Department of Oncology and Pathology, Karolinska Institute and Hospital in Stockholm.

Cell viability assay

During the experimental phase, the growth medium was replaced with complete media that contained the test substances at a concentration of 100 µg/ml. This was done in triplicate, after seeding 10,000 cells per well for the HOS cell line and 50,000 cells per well for BJ-1 in 96-well plates. Subsequently, the cells underwent this therapy for a duration of 48 h. For comparison purposes, the negative control consisted of a solution containing 0.5% DMSO, whereas the positive control contained 100 µg/ml of doxorubicin. Subsequently, following Mosmann's 1983 methodology, the MTT (3-(4,5-dimethylthiazol-2-yl)-2,5-diphenyltetrazolium bromide) assay was employed to assess the viability of the cells [53, 54]. The equation (Eq. 2) is utilized for the calculation of % cytotoxicity:

$$\%\text{Toxicity} = \left(\frac{av(X)}{av(NC)}\right) \times 100 \qquad (2)$$

where Av: average, X: absorbance of sample well measured at 595 nm with reference 690 nm, NC: absorbance of negative control measured at 595 nm with reference 690.

Determination of IC_{50} values

If the samples are extremely active and exhibit cytotoxicity of 75% or more on several cancer cell lines, different concentrations were generated for dose response studies [55]. The IC50 values of each sample were calculated using probity analysis and the SPSS computer program (SPSS for Windows, statistical analysis software package, version 9, 1989, SPSS Inc., Chicago, USA).

Author contributions

All authors contributed to conception and design of the study. Material preparation, data collection, and analysis were performed by WME, and materials preparation and characterizations were performed by AMB and HHS. The first draft of the manuscript was written by HHS and all authors commented and contributed to subsequent versions of the manuscript. All the antimicrobial tests were performed and analyzed by BH, while all cytotoxicity assessments were performed by AS. The final draft was edited and revised by WME.

Funding

Funding support was given by the National Research Centre, in-home project unit, project no. 13020238.

Data availability

All data are available when requesting by the reviewers.

Declarations

Conflict of interest The authors declare that they have no conflict of interest.

Ethical approval

The research carried out within this work did not involve human participants and/or animals.

Supplementary Information

The online version contains supplementary material available at https://doi.org/10.1557/s43578-024-01350-4.

References

1. H. Maleki-Ghaleh, M. Hossein Siadati, A. Fallah, A. Zarrabi, F. Afghah, B. Koc, E. Dalir Abdolahinia, Y. Omidi, J. Barar, A. Akbari-Fakhrabadi, Y. Beygi-Khosrowshahi, K. Adibkia, Effect of zinc-doped hydroxyapatite/graphene nanocomposite on the physicochemical properties and osteogenesis differentiation of 3D-printed polycaprolactone scaffolds for bone tissue engineering. Chem. Eng. J. **426**, 131321 (2021)
2. F. Hussain Alhamoudi, The role of fabrication methods and the impact of hydroxyapatite content on PU/HA scaffolds for tissue regeneration. J. Mater. Res. (2024). https://doi.org/10.1557/s43578-024-01288-7
3. R. Ghosh, S. Das, S.P. Mallick, Z. Beyene, A review on the antimicrobial and antibiofilm activity of doped hydroxyapatite and its composites for biomedical applications. Mater. Today Commun. **31**, 103311 (2022)
4. M.S. El Khooly, A.S. Abdraboh, A.M. Bakr, K.T. Ereiba, Fabrication and characterization of silver-substituted bioactiveglass incorporated with sodium alginate and graphene oxide. Mater. Chem. Phys. **301**, 127716 (2023)
5. A. Mahanty, D. Shikha, Microstructural, mechanical and biocompatibility investigation of metal-polymer-doped hydroxyapatite. J. Mater. Res. (2024). https://doi.org/10.1557/s43578-024-01297-6
6. A.A. Al-esnawy, K.T. Ereiba, A.M. Bakr, A.S. Abdraboh, Characterization and antibacterial activity of streptomycin sulfate loaded bioglass/chitosan beads for bone tissue engineering. J. Mol. Struct. **1227**, 129715 (2021)
7. M. Farrokhi-Rad, Effect of morphology on the electrophoretic deposition of hydroxyapatite nanoparticles. J. Alloys Compd. **741**, 211 (2018)
8. M. Gu, W. Li, L. Jiang, X. Li, Recent progress of rare earth doped hydroxyapatite nanoparticles: luminescence properties, synthesis and biomedical applications. Acta Biomater. **148**, 22 (2022)

9. H. Kaur, R. Garg, S. Singh, A. Jana, C. Bathula, H.-S. Kim, S.G. Kumbar, M. Mittal, Progress and challenges of graphene and its congeners for biomedical applications. J. Mol. Liq. (2022). https://doi.org/10.1016/j.molliq.2022.120703
10. K. Kadu, G. Ghosh, L. Panicker, M. Kowshik, S. Roy Ramanan, Role of surface charges on interaction of rod-shaped magnetic hydroxyapatite nanoparticles with protein. Colloid. Surf. B Biointerfaces **177**, 362 (2019)
11. M.S. El-khooly, A.S. Abdraboh, A.M. Bakr, K.H.T. Ereiba, Bioactivity and mechanical properties characterization of bioactive glass incorporated with graphene oxide. SILICON **15**(3), 1263 (2023)
12. H. Kim, S. Mondal, B. Jang, P. Manivasagan, M.S. Moorthy, J. Oh, Biomimetic synthesis of metal–hydroxyapatite (Au-HAp, Ag-HAp, Au-Ag-HAp): structural analysis, spectroscopic characterization and biomedical application. Ceram. Int. **44**(16), 20490 (2018)
13. Y. Wu, S. Chen, P. Luo, S. Deng, Z. Shan, J. Fang, X. Liu, J. Xie, R. Liu, S. Wu, X. Wu, Z. Chen, K.W.K. Yeung, Q. Liu, Z. Chen, Optimizing the bio-degradability and biocompatibility of a biogenic collagen membrane through cross-linking and zinc-doped hydroxyapatite. Acta Biomater. **143**, 159 (2022)
14. C.-D. Deng, Z.-Q. Gong, S.-L. Wang, W. Song, Y.-L. Zhang, T.-T. Yan, A novel calcium phosphate cement used for enhanced pedicle screw fixation: a biomechanical study with finite element. J. Mater. Res. (2022). https://doi.org/10.1557/s43578-022-00722-y
15. D.M. Vranceanu, E. Ungureanu, I.C. Ionescu, A.C. Parau, A.E. Kiss, A. Vladescu, C.M. Cotrut, Electrochemical surface biofunctionalization of titanium through growth of TiO_2 nanotubes and deposition of Zn doped hydroxyapatite. Coatings **12**(1), 69 (2022)
16. R. Sergi, D. Bellucci, R.T. Candidato, L. Lusvarghi, G. Bolelli, L. Pawlowski, G. Candiani, L. Altomare, L. De Nardo, V. Cannillo, Bioactive Zn-doped hydroxyapatite coatings and their antibacterial efficacy against *Escherichia coli* and *Staphylococcus aureus*. Surf. Coat. Technol. **352**, 84 (2018)
17. K.P. Tank, K.S. Chudasama, V.S. Thaker, M.J. Joshi, Pure and zinc doped nano-hydroxyapatite: synthesis, characterization, antimicrobial and hemolytic studies. J. Cryst. Growth **401**, 474 (2014)
18. A. Kaur, M. Kaur, P. Vyas, V. Singh, Structural and optical studies on Ti 4+ and Mg 2+-substituted strontium ferrite nanoparticles for enhancing visible-light-driven photocatalytic and antimicrobial activity The effect of Ti 4+ and Mg 2+ substitution on the structural, optical, photocatalytic, and antimicrobial activity of strontium ferrite NPs was comprehensively studied. The ratio of Ti 4+ and Mg 2+ ions was varied in Sr 0.4 Ti 0.6-x Mg x Fe 2 O 4+δ (x = 0). J. Mater. Res. **39**, 590–608 (2024)
19. C. Bathula, R. Mk, A. Kumar, H. Yadav, S. Ramesh, S. Shinde, N.K. Shrestha, M. Km, V. Reddy, A. Mohammed, Microwave assisted synthesis of imidazolyl fluorescent dyes as antimicrobial agents. J. Mater. Res. Technol. (2020). https://doi.org/10.1016/j.jmrt.2020.01.011
20. S. Khadtare, A.S. Bansode, V.L. Mathe, N.K. Shrestha, C. Bathula, S.-H. Han, H.M. Pathan, Effect of oxygen plasma treatment on performance of ZnO based dye sensitized solar cells. J. Alloys Compd. (2017). https://doi.org/10.1016/j.jallcom.2017.07.013
21. A.N. Kadam, D.P. Bhopate, V.V. Kondalkar, S.M. Majhi, C.D. Bathula, A.-V. Tran, S.-W. Lee, Facile synthesis of Ag-ZnO core-shell nanostructures with enhanced photocatalytic activity. J. Ind. Eng. Chem. (2017). https://doi.org/10.1016/j.jiec.2017.12.003
22. I. Uysal, B. Yilmaz, Z. Evis, Zn-doped hydroxyapatite in biomedical applications. J. Aust. Ceram. Soc. **57**(3), 869 (2021)
23. A.M.E. Nahrawy, A.M. Bakr, A.B.A. Hammad, A.M. Mansour, Nano-architecture of CaO/Ag-chitosan nanocomposite by sol gel process: formation and characterization. Egypt. J. Chem. **64**(12), 7393 (2021)
24. Y. Wang, F. Gao, L. Zhao, Y. Wu, C. Li, H. Li, Y. Jiang, Enhancing cancer treatment via "Zn^{2+} interference" with Zn-based nanomaterials. Coord. Chem. Rev. **500**, 215535 (2024)
25. Y. Su, I. Cockerill, Y. Wang, Y.-X. Qin, L. Chang, Y. Zheng, D. Zhu, Y. Zheng, D. Zhu, Zinc-based biomaterials for regeneration and therapy. Trends Biotechnol. (2019). https://doi.org/10.1016/j.tibtech.2018.10.009
26. S. Wu, K. Zhang, Y. Liang, Y. Wei, J. An, Y. Wang, J. Yang, H. Zhang, Z. Zhang, J. Liu, J. Shi, S. Wu, K. Zhang, Y. Liang, Y. Wei, J. An, Y. Wang, J. Yang, H. Zhang, Z. Zhang, J. Liu, J. Shi, Adv. Sci. (2021). https://doi.org/10.1002/advs.202103534
27. C. Abildgaard, P. Guldberg molecular drivers of cellular metabolic reprogramming in melanoma. (n.d.).
28. J. Wang, C. Qu, X. Shao, G. Song, J. Sun, D. Shi, R. Jia, H. An, H. Wang, Carrier-free nanoprodrug for p53-mutated tumor therapy via concurrent delivery of zinc-manganese dual ions and ROS. Bioact. Mater. **20**, 404 (2023)
29. J. Yan, C. Liu, Q. Wu, J. Zhou, X. Xu, L. Zhang, D. Wang, F. Yang, H. Zhang, Mineralization of pH-sensitive doxorubicin prodrug in ZIF-8 to enable targeted delivery to solid tumors. Anal. Chem. **92**(16), 11453 (2020)
30. Q. Yu, Q. Li, L. Tu, Y. Zhou, H. Zhu, Q. Zhang, M. Liu, Y. Sun, Calcium sulfide based nanoreservoirs elicit dual pyroptosis pathways for enhanced anti-tumor immunity. Chem. Eng. J. **477**, 147085 (2023)
31. G.E. Poinern, R.K. Brundavanam, N. Mondinos, Z.T. Jiang, Synthesis and characterisation of nanohydroxyapatite using an ultrasound assisted method. Ultrason. Sonochem. **16**(4), 469 (2009)
32. D. Gopi, J. Indira, L. Kavitha, M. Sekar, U.K. Mudali, Synthesis of hydroxyapatite nanoparticles by a novel ultrasonic assisted with mixed hollow sphere template method. Spectrochim. Acta Part A Mol. Biomol. Spectrosc. **93**, 131 (2012)
33. D. Venkatasubbu, G. Avadhani, R. Thangavel, J. Kumar: 72 Publications 2561 Citations See Profile (n.d.).

34. G.D. Venkatasubbu, S. Ramasamy, G.S. Avadhani, L. Palanikumar, J. Kumar, Size-mediated cytotoxicity of nanocrystalline titanium dioxide, pure and zinc-doped hydroxyapatite nanoparticles in human hepatoma cells. J. Nanoparticle Res. (2012). https://doi.org/10.1007/s11051-012-0819-3
35. W. El Hotaby, A.M. Bakr, H.S. Ibrahim, N.S. Ammar, H.A. Hani, A.A. Mostafa, Eco-friendly zeolite/alginate microspheres for Ni ions removal from aqueous solution: kinetic and isotherm study. J. Mol. Struct. **1241**, 130605 (2021)
36. I. Uysal, F. Severcan, A. Tezcaner, Z. Evis, Co-doping of hydroxyapatite with zinc and fluoride improves mechanical and biological properties of hydroxyapatite. Progress Nat. Sci. Mater. Int. **24**(4), 340 (2014)
37. Y. Bi, M. Huang Characterization and Analysis of nano-hydroxy apatite material. **582** (2015)
38. A. Turlybekuly, A.D. Pogrebnjak, L.F. Sukhodub, L.B. Sukhodub, A.S. Kistaubayeva, I.S. Savitskaya, D.H. Shokatayeva, O.V. Bondar, Z.K. Shaimardanov, S.V. Plotnikov, B.H. Shaimardanova, I. Digel, Synthesis, characterization, in vitro biocompatibility and antibacterial properties study of nanocomposite materials based on hydroxyapatite-biphasic ZnO micro- and nanoparticles embedded in Alginate matrix. Mater. Sci. Eng. C **104**, 109965 (2019)
39. C.Y. Beh, E.M. Cheng, N.F. Mohd Nasir, S.F. Khor, S.K. Eng, M.S. Abdul Majid, M.J.M. Ridzuan, K.Y. Lee, Low frequency dielectric and optical behavior on physicochemical properties of hydroxyapatite/cornstarch composite. J. Colloid Interface Sci. **600**, 187 (2021)
40. M.M.H. El-Sayed, A.A. Mostafa, A.M. Gaafar, W. El Hotaby, E.M.A. Hamzawy, M.S. El-Okaily, A.M. Gamal-Eldeen, In vitro kinetic investigations on the bioactivity and cytocompatibility of bioactive glasses prepared via melting and sol–gel techniques for bone regeneration applications. Biomed. Mater. **12**(1), 015029 (2017)
41. K.R. Mohamed, H.H. Beherei, G.T. El Bassyouni, N. El Mahallawy, Fabrication and mechanical evaluation of hydroxyapatite/oxide nano-composite materials. Mater. Sci. Eng. C **33**(7), 4126 (2013)
42. H. Gheisari, E. Karamian, Preparation and characterization of hydroxyapatite reinforced with hardystonite as a novel bio-nanocomposite for tissue engineering. Nanomed. J. **2**(2), 141 (2015)
43. S. Sibte, A. Abidi, Q. Murtaza, Synthesis and characterization of nano-hydroxyapatite powder using wet chemical precipitation reaction. J. Mater. Sci. Technol. (2013). https://doi.org/10.1016/j.jmst.2013.10.011
44. G. Mahmutoglu, A. Topsakal, E. Altan, N. Kuskonmaz, S. Dagli-lar, F.N. Oktar, G. Erdemir, S.E. Kuruca, S. Akyol, O. Gunduz, B. Ben-Nissan, Effects of temperature and pH on the synthesis of nanohydroxyapatite powders by chemical precipitation. J. Aust. Ceram. Soc. **59**(5), 1433 (2023)
45. C. Oliveira De Lima, A.L. Menezes De Oliveira, L. Chantelle, E.C.S. Filho, M. Jaber, M.G. Fonseca, 111471-Tour 23, 3` emé etage, couloir 23–33. Colloids Surf. B Biointerfaces **198**, 75005 (2021)
46. S. Mardin, E.M.A. Hamzawy, A. Abd El Aty, G.T. El-Bassyouni, Zn-containing wollastonite with well-defined microstructural and good antifungal activity. SILICON **15**(11), 4653 (2023)
47. W. Akram, R. Zahid, R.M. Usama, S.A. AlQahtani, M. Dahshan, M.A. Basit, M. Yasir, Enhancement of antibacterial properties, surface morphology and in vitro bioactivity of hydroxyapatite-zinc oxide nanocomposite coating by electrophoretic deposition technique. Bioengineering **10**(6), 693 (2023)
48. N. Ohtsu, Y. Kakuchi, T. Ohtsuki, Antibacterial effect of zinc oxide/hydroxyapatite coatings prepared by chemical solution deposition. Appl. Surf. Sci. (2017). https://doi.org/10.1016/j.apsusc.2017.09.101
49. A.M. Bakr, B. Anis, W. Hotaby, Sounchemical synthesis of graphene/nano hydroxyapatite composites for potential biomedical application. Egypt. J. Chem. **65**(2), 669 (2022)
50. G.W. Ali, W. El-Hotaby, B. Hemdan, W.I. Abdel-Fattah, Thermo-sensitive chitosan/phosphate hydrogel-composites fortified with Ag versus Ag@Pd for biomedical applications. Life Sci. **194**, 185 (2018)
51. W.A. Khalil, H.H.A. Sherif, B.A. Hemdan, S.K.H. Khalil, W. El Hotaby, Biocompatibility enhancement of graphene oxide-silver nanocomposite by functionalisation with polyvinylpyrrolidone. IET Nanobiotechnol. **13**(8), 816 (2019)
52. S.T. Gaballah, H.A. El-Nazer, R.A. Abdel-Monem, M.A. El-Liethy, B.A. Hemdan, S.T. Rabie, Synthesis of novel chitosan-PVC conjugates encompassing Ag nanoparticles as antibacterial polymers for biomedical applications. Int. J. Biol. Macromol. **121**, 707 (2019)
53. T. Mosmann, Rapid colorimetric assay for cellular growth and survival: application to proliferation and cytotoxicity assays. J. Immunol. Methods **65**(1–2), 55 (1983)
54. H.H.A. Sherif, W. El Hotaby, S.K.H. Khalil, B.A. Hemdan, W.A. Khalil, Preparation, characterization, and biological assessment of functionalized reduced graphene oxide–silver nanocomposite. J. Mater. Res. **38**(7), 1843 (2023)
55. C. Bézivin, S. Tomasi, F. Lohezic-Le Devehat, J. Boustie, Cytotoxic activity of some lichen extracts on murine and human cancer cell lines. Phytomedicine **10**(6–7), 499 (2003)